

Impact of symmetric vs asymmetric conjugated extensions in acceptors on the photovoltaic performance of organic solar cells

Jie Wang^{a,1}, Xin Chen^{a,1}, Wenkai Zhao^b, Jiong Yang^a, Guankui Long^b, Zhaoyang Yao^a, Chenxi Li^a, Xiangjian Wan^{a,*}, Yongsheng Chen^{a,*}

^a State Key Laboratory of Elemento-Organic Chemistry, Frontiers Science Center for New Organic Matter, The Centre of Nanoscale Science and Technology and Key Laboratory of Functional Polymer Materials, Institute of Polymer Chemistry, Renewable Energy Conversion and Storage Center (RECAST), Tianjin Key Laboratory of Functional Polymer Materials, Nankai University, Tianjin 300071, China

^b School of Materials Science and Engineering, National Institute for Advanced Materials, Nankai University, Tianjin 300071, China

ARTICLE INFO

Keywords:

Organic solar cells
Non-fullerene acceptors
Energy loss
Asymmetric
Symmetric

ABSTRACT

To enhance efficiencies of organic solar cells (OSCs), it is essential to minimize the energy loss (E_{loss}) or maximize open-circuit voltage (V_{oc}) while ensuring that the short-circuit current density (J_{sc}) and fill factor (FF) are not sacrificed. In this work, we designed two small-molecule acceptors (SMAs), named CHSPH and CHAPH, which incorporate fused 2-bromobenzene units symmetrically and asymmetrically within the central unit of the Y-series SMAs. The asymmetric π -extending 2-bromobenzene block enhances π - π stacking, thereby facilitating efficient charge transport and improving luminous efficiency while minimizing non-radiative recombination. As a result, CHAPH demonstrates a significantly reduced non-radiative energy loss (ΔE_{nr}) of 0.180 eV and E_{loss} of 0.508 eV. Consequently, OSCs based on CHAPH achieve a power conversion efficiencies (PCE) of 19.35 %, representing a substantial improvement over the 10.06 % PCE of OSCs based on CHSPH. This result provides a promising molecular strategy for enhancing the performance of high-efficiency OSCs.

1. Introduction

Organic solar cells (OSCs) have attracted significant attention due to their flexibility, lightweight nature, and capability for large-area fabrication [1–4]. Recent advancements in active layer materials, particularly non-fullerene acceptors (NFAs) with an acceptor-donor-acceptor (A-D-A) structure, such as ITIC and Y-series, have led to rapid progress in OSCs, achieving power conversion efficiencies (PCEs) exceeding 20 % in single-junction devices [5–10]. This progress has narrowed the efficiency gap between OSCs and inorganic or perovskite solar cells. Currently, OSCs can achieve high short-circuit current densities (J_{sc}) surpassing 28 mA cm⁻², fill factors (FF) over 80 %, and external quantum efficiency (EQE) values approaching 85 %. However, OSCs still exhibit relatively lower open-circuit voltages (V_{oc}) compared to inorganic and perovskite counterparts, primarily due to higher energy losses (E_{loss}), typically exceeding 0.53 eV [11–15]. In OSCs, E_{loss} mainly arises from the driving force required for exciton dissociation and nonradiative charge recombination. To minimize E_{loss} , several strategies have been proposed: modifying molecular polarizability to reduce exciton binding

energy, thereby lowering the driving force for exciton dissociation; managing energetic disorder through molecular design or optimizing morphology to balance charge carrier transport and recombination; and reducing nonradiative recombination by decreasing intermolecular interactions induced by electrostatic potentials [16–24]. Furthermore, considerable efforts have been directed toward precisely controlling the morphology of the active layer to improve V_{oc} , J_{sc} , and FF. Molecular characteristics, such as dipole moment, crystallinity, electrostatic potentials, and compatibility with donor materials, are carefully adjusted to establish an optimal morphology with appropriate phase separation and a bicontinuous interpenetrating network. Despite these efforts, it remains challenging for simultaneously reducing E_{loss} and optimizing morphology to enhance V_{oc} without compromising J_{sc} and FF [25–31].

In recent years, we and other groups have designed a series of acceptors using a central core extended conjugation strategy based on Y-series acceptors, which offers advantages such as stronger intermolecular interactions, improved carrier transport, and reduced reorganization energy [32–35]. Particularly, the configuration of these acceptors has proved to favorable to minimize E_{loss} and enhance the V_{oc} . Recently,

* Corresponding authors.

E-mail addresses: xjwan@nankai.edu.cn (X. Wan), yschen99@nankai.edu.cn (Y. Chen).

¹ These authors contributed equally.

<https://doi.org/10.1016/j.nanoen.2025.111028>

Received 11 February 2025; Received in revised form 21 March 2025; Accepted 14 April 2025

Available online 14 April 2025

2211-2855/© 2025 Elsevier Ltd. All rights are reserved, including those for text and data mining, AI training, and similar technologies.

we have found that brominating the central unit can improve intermolecular stacking, crystallinity, and the dielectric constant [36]. The device based on CH21 achieved a PCE of 18.12 %, with a V_{oc} of 0.873 V, J_{sc} of 26.57 mA cm^{-2} , and a FF of 78.13 %. The OSC based on CH22 further reached a PCE of 19.06 %, with a V_{oc} of 0.884 V, a J_{sc} of 26.74 mA cm^{-2} , and an impressive FF of 80.62 %. This represents one of the highest PCE for OSCs based on the Y-series acceptors with central core conjugated extension. However, CH21 and CH22 still exhibit relatively large E_{loss} values of 0.525 eV and 0.530 eV, respectively. In this work, in order to further minimize E_{loss} or enhance the V_{oc} , while maintaining excellent J_{sc} and FF, we designed and synthesized two acceptors, CHSPH and CHAPH (Fig. 1a) via further π -extending in central units of CH21 and CH22. Experimental and computational results demonstrate that symmetric or asymmetric conjugation extensions in the central unit significantly affect the inherent molecular properties, including electrostatic potential, donor compatibility, polarity, light-harvesting ability, and aggregation behavior. Each of these factors profoundly impacts the blend morphology, subsequently affecting photovoltaic performance. Compared to PM6:CHSPH, the blend film of PM6:CHAPH demonstrated a uniform and appropriately sized fiber network morphology. These

improvements facilitate charge generation, transport, and collection while minimizing E_{loss} in OSCs. The CHAPH-based binary devices exhibit an impressive ΔE_{nr} of 0.180 eV, achieving of the 19.35 % highest PCE, with a higher V_{oc} of 0.912 V, J_{sc} of 26.9 mA cm^{-2} , and an FF of 79.09 %. This study underscores the significance of asymmetric fusion extension for SMAs and highlights the pathway towards the development of OSCs with low E_{loss} and high PCE.

2. Results and discussion

2.1. Design and optoelectronic characterization

The chemical structures of CH21, CH22, CHSPH, and CHAPH are shown in Fig. 1a. The synthetic routes of the CHSPH and CHAPH are depicted in Scheme S1-S5 and characterizations, such as ^1H NMR, ^{13}C NMR, and high-resolution mass spectrometry (HRMS) results are provided in the Supporting Information (SI). To assess the thermal stability of two SMAs, thermogravimetric analysis (TGA) was performed in a nitrogen environment. As shown in Figure S1(SI), CHSPH and CHAPH demonstrate good thermal stability with decomposition temperature

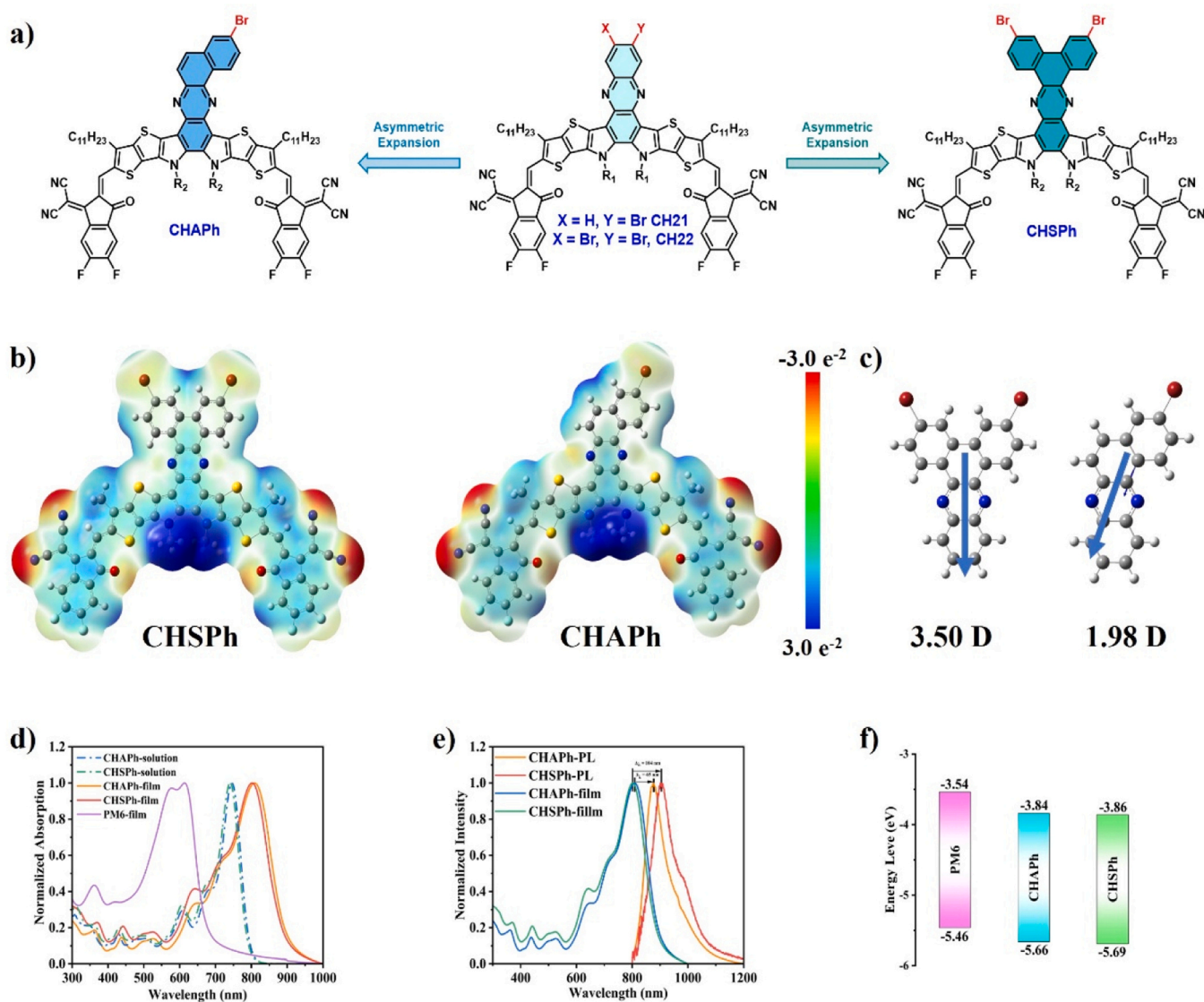


Fig. 1. a) Molecular structures of CH21, CH22, CHSPH, and CHAPH. b) Electrostatic surface potential (ESP) maps for CHSPH and CHAPH. c) Local dipole moment of two SMAs. d) Normalized UV-vis absorption spectra of the two SMAs in chloroform and film, with polymer donor PM6 in films. e) UV-vis absorption and photoluminescence (PL) spectra of two SMAs in the films. f) Energy level diagram of the PM6 and two SMAs.

(T_d) of 338°C and 332°C, respectively.

To investigate the molecular structure characteristics, we employed density functional theory (DFT) calculations to analysis the optimized single-molecule geometry and local dipole moment of the two SMAs. Based on the optimized geometries in Figure S2(SI), the two acceptors exhibit similar N–C–N dihedral angles of 8.39° and 8.40° at the central unit, respectively, suggesting good molecular planarity for CHSPH and CHAPH. Additionally, DFT calculations were used to analyze the electrostatic surface potential (ESP) diagrams for the two acceptors depicted in Fig. 1c. The fused 2-bromobenzene within the central shows a more negative electrostatic surface potential, and the dipole moment of the central unit increases from CHAPH to CHSPH (Fig. 1d). However, the direction of the molecular dipole moments for CHSPH and CHAPH differ significantly, which suggests that the fused 2-bromobenzene in the central unit significantly modifies intermolecular interactions and affects both acceptors packing and surface energy. In practice, CHSPH and CHAPH exhibit distinct stacking mode within the films, which will be further discussed in the morphology section.

The UV–visible absorption spectra of two SMAs are shown in Fig. 1e. In dilute chloroform solution, the fused 2-bromobenzene block reduces the electron-donating ability of the central unit, resulting in a slight blue shift (~4 nm) in the absorption spectrum of CHSPH compared to CHAPH, which exhibits λ_{\max} values of 741 nm and 745 nm, respectively. In films, CHSPH and CHAPH show red shifts of 61 nm and 64 nm, with λ_{\max} values of 802 nm and 809 nm. The absorption spectra of D/A blend films (Figure S3, SI) reveals that two SMAs have broad absorption in the 300–900 nm. Notably, the acceptor absorption peak in the PM6:CHSPH blend is significantly weaker than that of the donor, primarily attributed to the irregular arrangement of CHSPH in the film, reduced intermolecular interactions and energy transfer efficiency lead to a decrease in the light absorption capability of the CHSPH. The Stokes shift ($\Delta\lambda_{\text{stokes}}$) for CHSPH and CHAPH is 104 nm and 65 nm, respectively (Fig. 1f). Therefore, the smaller $\Delta\lambda_{\text{stokes}}$ in CHAPH suggests enhanced exciton diffusion and reduced non-radiative recombination, both of which are advantageous for minimizing ΔE_{nr} in OSCs. The energy levels of CHSPH and CHAPH were determined via electrochemical cyclic voltammetry (CV). The CV curves (Figure S4, SI) show the LUMO and HOMO energy levels of the two acceptors, as illustrated in Fig. 1g. Specifically, the LUMO/HOMO values of CHSPH is –3.86/–5.69 eV, and the LUMO/HOMO values of CHAPH is –3.84/–5.66 eV. The increase of the electron-withdrawing 2-bromophenyl block into the central until results in a slight decrease in both the LUMO and HOMO. Compared to CHSPH, the electron density increase in the CHAPH central unit reduces the intramolecular charge transfer (ICT) effect, The upshift LUMO energy level is beneficial for improving the V_{oc} of the OSCs. This trend is consistent with the DFT calculations, which predict the LUMO/HOMO values of CHSPH is –3.58/–5.63 eV and for CHAPH is –3.54/–5.57 eV (Figure S5, SI).

2.2. Photovoltaic performance

OSC devices with a structure of ITO/2PACz/PM6:acceptor/PNDIT-F3N/Ag were fabricated[37]. The fabrication methods of the OSCs are presented in SI and the related results are summarized in Table 1. The corresponding J – V and EQE curves of the optimal devices are shown in

Table 1
Photovoltaic parameters of the optimized binary devices.

Devices	V_{oc} [V]	J_{sc} [mA cm ⁻²]	FF [%]	$J_{\text{sc,cal}}^a$ [mA cm ⁻²]	PCE [%] ^b
CHSPH	0.884	17.89	63.64	15.52	10.06 (9.80 ± 0.62)
CHAPH	0.912	26.91	79.03	26.08	19.35 (19.23 ± 0.11)

^a)Current densities are calculated from EQE curves; ^b) Statistical and optimal results are listed in parentheses and outside parentheses, respectively. The average parameters were computed from 8 independent devices.

Fig. 2a-b. A comparison of the related photovoltaic parameters for the binary OSCs can be seen in Fig. 2c. The OSCs based on PM6:CHSPH exhibit a low PCE of 10.06 % with a J_{sc} of 17.89 mA cm⁻², an FF of 63.64 %, and a low V_{oc} of 0.884 V. In contrast, OSCs based on PM6:CHAPH exhibit superior photovoltaic performance with a PCE of 19.35 %, significantly improved J_{sc} of 26.91 mA cm⁻², an FF of 79.03 %, and a high V_{oc} of 0.912 V. Moreover, the J_{sc} values integrated from the EQE curves closely match the J_{sc} values acquired from the J – V tests. The CHAPH-based OSCs exhibited broad and strong photoelectric responses from 350 to 850 nm, with the EQE edge surpassing 900 nm and intensity approaching 85 % within the 480–660 nm segment, indicating efficient charge generation across this spectrum, resulting in the desired J_{sc} of 26.91 mA cm⁻².

2.3. Energy loss analysis

The devices based on PM6:CHAPH exhibit a significantly higher V_{oc} of 0.912 V compared to the PM6:CHSPH of 0.884 V. Given that the E_{LUMO} values of CHSPH and CHAPH are very close, the substantial difference in V_{oc} between may be attributed to differences in E_{loss} . We have conducted the E_{loss} analysis and the detailed results are listed in Table 2. According to the Shockley-Queisser (SQ) theory, the E_{loss} in OSCs can be divided into three parts, $E_{\text{loss}} = q\Delta V_{\text{oc}} = E_{\text{g}} - qV_{\text{oc}} = \Delta E_1 + \Delta E_2 + \Delta E_3$, where E_{g} is the bandgap energy, q is the charge of an electron [38]. The E_{loss} is attributed to three distinct contributions: ΔE_1 , ΔE_2 , and ΔE_3 . ΔE_1 represents the portion of photon energy above the material's absorption threshold that cannot be utilized. The optical absorption properties of the material determine the energy range and efficiency of the absorbed photons [39]. Since the absorption spectra of CHSPH and CHAPH are similar, their ΔE_1 values are also close, measured at 0.264 eV and 0.265 eV, respectively. ΔE_2 (or ΔE_r) primarily arises during the charge separation process due to the energy level mismatch at the donor-acceptor interface, where electron and hole transfer must overcome the energy level difference [40]. Additionally, charge recombination at the interface may occur, leading to the release of the absorbed photon energy. The energy level structure of the acceptor material determines the interface energy level difference, and poor level alignment results in an increased ΔE_2 . Since CHSPH and CHAPH have similar E_{LUMO} , they exhibit nearly identical ΔE_2 values of 0.066 eV and 0.063 eV, respectively.

ΔE_3 (or ΔE_{nr}) represents non-radiative recombination and is calculated $\Delta E_{\text{nr}} = q(V_{\text{oc}}^{\text{rad}} - V_{\text{oc}})$ or $q\Delta E_{\text{nr}} = -kT\ln(\text{EQE}_{\text{EL}})$, where $V_{\text{oc}}^{\text{rad}}$ is the V_{oc} when there is only radiative recombination and EQE_{EL} refers to the radiative quantum efficiency of the device under dark charge carrier injection [41]. ΔE_{nr} primarily occurs during the charge transport process, where defects form trap states in the active layer that capture charges, leading to a decrease in charge transport efficiency. Additionally, scattering of charges by phonons and molecular vibrations increases the path length and time of charge transport, thereby raising the probability of recombination. Recent studies indicate that improving the photoluminescence quantum yield (PLQY) of acceptor materials plays a key role in reducing ΔE_{nr} [42]. Since CHSPH has a PLQY of 4.54 %, significantly lower than CHAPH's 6.79 % (Figure S6, SI), the blend of PM6:CHSPH exhibits a lower EQE_{EL} value (4.5×10^{-4}), while the blend of PM6:CHAPH shows an EQE_{EL} value of 6.2×10^{-4} (Fig. 2e). As a result, the blend of PM6:CHAPH shows a significantly reduced non-radiative recombination, with a ΔE_{nr} value of only 0.180 eV. In contrast, the blend of PM6:CHSPH has a relatively higher ΔE_{nr} value of 0.196 eV. Benefiting from the significantly reduced ΔE_{nr} , the E_{loss} in devices based on CHAPH is reduced to 0.508 eV, while for PM6:CHSPH, it is 0.526 eV. A comprehensive analysis of the E_{loss} for two acceptor indicates that asymmetric fused extension in the central unit of the acceptor material can effectively reduce ΔE_{nr} .

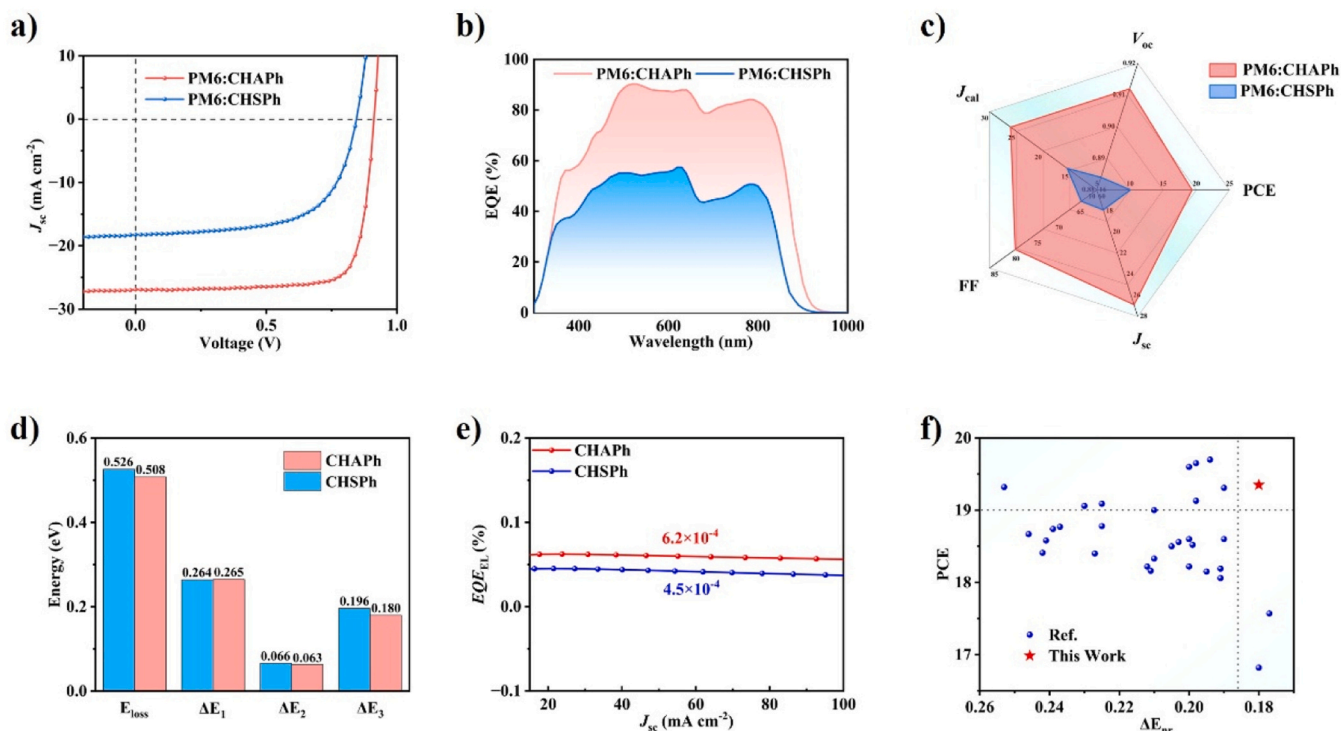


Fig. 2. a, b) J - V and EQE curve for the optimized devices. c) Parameter comparison for the binary OSCs. d, e) E_{loss} diagram and EQE_{EL} spectra for the optimized devices. f) ΔE_{nr} vs PCE (over 15 %) for binary OSCs with SMAs.

Table 2

Total energy loss values and different contributions in solar cells based on the SQ limit theory.

Active later	V_{oc} [V]	E_{g} ^{a)} [eV]	$V_{\text{OC}}^{\text{SQ}}$ ^{b)} [V]	$V_{\text{OC}}^{\text{rad}}$ ^{c)} [V]	$\Delta E_1^{\text{d)}$ [eV]	ΔE_r [eV]	$\Delta E_{\text{nr}}^{\text{e)}$ [eV]	ΔE_{nr} ^{f)} [eV]	$E_{\text{loss}}^{\text{g)}$ [eV]
PM6:CHSPh	0.884	1.41	1.146	1.080	0.264	0.066	0.196	0.199	0.526
PM6:CHAPh	0.912	1.42	1.155	1.092	0.265	0.063	0.180	0.191	0.508

^{a)} E_{g} was estimated via the crossing points between normalized absorption and PL spectra of films; ^{b)} $V_{\text{OC}}^{\text{SQ}}$ is calculated according to the SQ limit; ^{c)} $V_{\text{OC}}^{\text{rad}}$ is the V_{OC} when there is only radiative recombination and are calculated from sEQE measurements. ^{d)} $\Delta E_1 = E_{\text{g}} - V_{\text{OC}}^{\text{SQ}}$; ^{e)} ΔE_{nr} obtained from the equation $\Delta E_{\text{nr}} = q(V_{\text{OC}}^{\text{rad}} - V_{\text{OC}})$. ^{f)} ΔE_{nr} obtained from the equation $q\Delta E_{\text{nr}} = -kT\ln(\text{EQE}_{\text{EL}})$ by measuring the device EQE_{EL} . ^{g)} $E_{\text{loss}} = E_{\text{g}} - V_{\text{OC}}$.

2.4. Morphology analysis

In addition to the rational design of molecular structures, achieving an optimal phase morphology characterized by a moderate phase separation is crucial for the fabrication of high-efficiency OSCs. Atomic force microscopy (AFM) and grazing-incidence wide-angle X-ray scattering (GIWAXS) measurements were conducted to analyze the surface (Fig. 3a-f) and bulk morphologies (Fig. 3g-k) of photoactive layers based on CHSPh and CHAPh [43]. As illustrated in Fig. 3a, the blend films of PM6:CHSPh exhibit a relatively rough surface morphology, with a root-mean-square (RMS) roughness of 0.92 nm. In contrast, the RMS roughness for the PM6:CHAPh blend film is 0.76 nm (Fig. 3d). The good crystallinity of CHAPh facilitates the formation of more uniform and appropriately sized acceptor domains (Fig. 3e), providing sufficient interfacial area for efficient exciton dissociation. This inhibits the excessive enlargement of the acceptor domains, which could otherwise increase the electron transport distance or enhance recombination. In contrast, the poor crystallinity of CHSPh leads to incomplete phase separation, resulting in larger disordered regions and areas of excessive crystallization (Fig. 3d), which hinder the effective transport of electrons, thereby reducing device efficiency. Additionally, the AFM phase images (Figure S7, S1) illustrate well-defined interpenetrating microstructures of nanofibers in the PM6:CHAPh blended films, which create

efficient bi-continuous pathways for the transport of holes and electrons.

The arrangement of donor and acceptor materials in a face-on configuration, which showcases strong π - π stacking, is essential for efficient carrier transport. In the 2D-GIWAXS images of the neat CHSPh film (Fig. 3g), the presence of bright diffraction rings with comparable intensity across random directions indicates the formation of a strongly aggregated mixed orientation architecture, where molecules are randomly oriented in multiple directions. This observation suggests substantial intermolecular π - π stacking interactions, likely originating from the rigid planar structure of the conjugated backbone [44]. Meanwhile, no clear diffraction peaks were observed in the out-of-plane (OOP) direction for the PM6:CHSPh blend film, indicating the absence of long-range ordered structures parallel to the substrate. In contrast, the CHAPh and PM6:CHAPh films exhibited clear diffraction halos in the q_z direction, indicating more ordered molecular arrangements, which are beneficial for vertical electron and hole transport. Tangential profile analysis of the OOP direction revealed that the d-spacing values for CHAPh and PM6:CHAPh films were 3.65/3.70 Å, with crystal coherence lengths (CCL) of 20.2/25.7 Å, respectively, demonstrating better molecular order. In the in-plane (IP) direction, PM6:CHSPh blend films exhibited the highest CCL of 77.46 Å and 122.93 Å, significantly higher than those of CHAPh and PM6:CHAPh blend films (21.42 Å and 77.46 Å). 2D GIWAXS results reveal that the symmetry and asymmetry

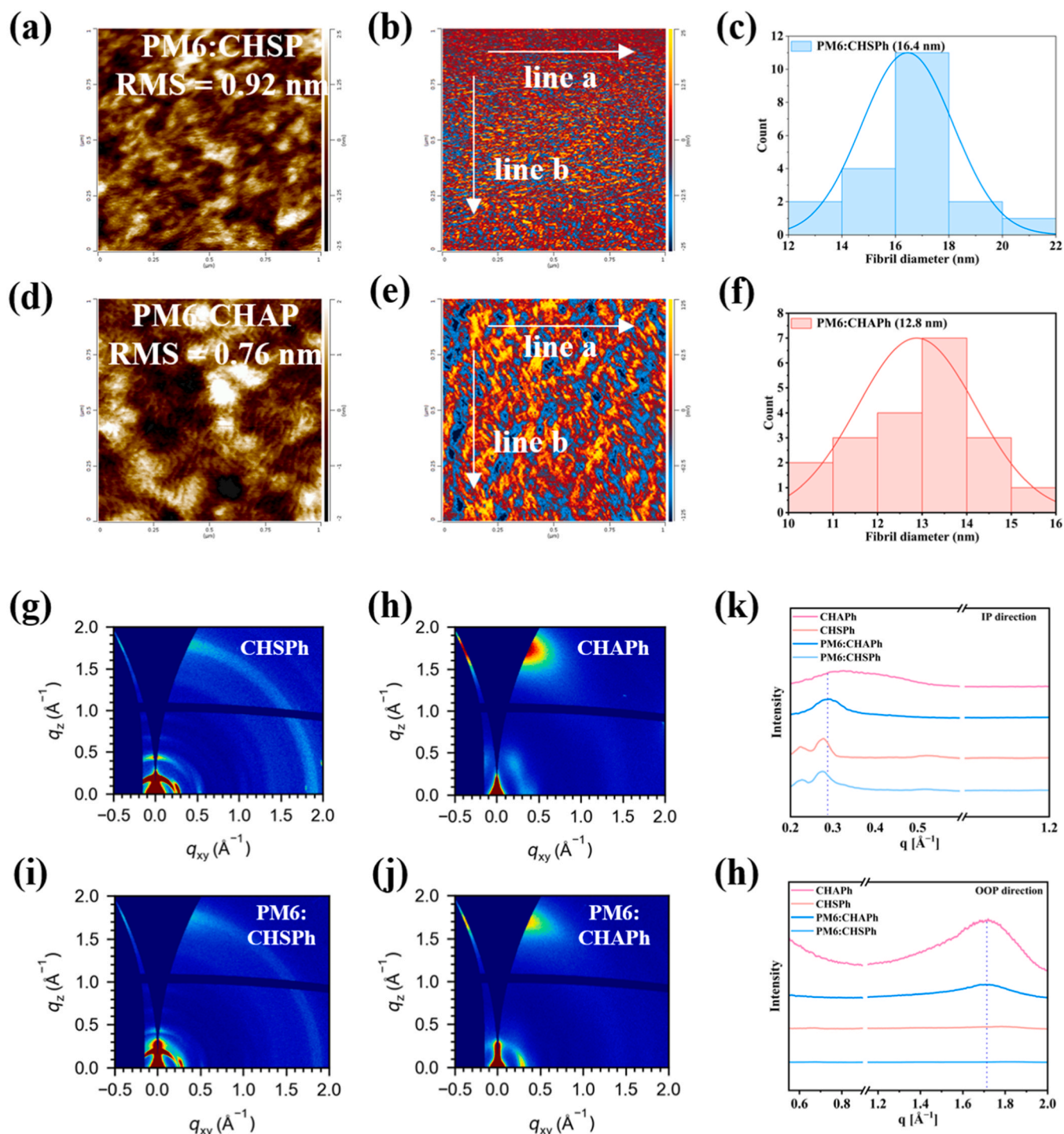


Fig. 3. a-f) AFM height, IR images and fibril diameter of blend films; g-l) 2D GIWAX images, IP and OOP line-cut profiles of two acceptors neat and blend film.

fused 2-bromophenyl in central unit of two acceptor have a significant impact on molecular packing, crystallization behavior, and aggregation states, which ultimately influence the performance of photovoltaic devices.

We calculated the surface energy (SE) and the Flory–Huggins interaction parameter (χ) for donor and acceptor from the contact angle (CA) test (Figure S8 and Table S6, SI). The SE values for PM6, CHSP, and CHAP were determined to be 31.28, 29.46, and 37.12 mN m⁻¹, respectively. A closer SE indicates improved miscibility between the donor and acceptor materials. By employing the empirical formula $\chi_{D:A} = K(\sqrt{\gamma_D} - \sqrt{\gamma_A})^2$, where K represents a constant and γ_D/γ_A signifies the

SE of the donor and acceptor, we calculated the interaction parameters χ for the blend films of PM6-CHSP and PM6-CHAP to be 0.25 K and 0.03 K, respectively. The decrease of χ in the blend film indicates an improvement in the miscibility between the donor and acceptor, attributed to the decrease fused 2-bromobenzene in the central. This enhancement may result from an increase in crystallinity, which expands the interaction region, as demonstrated by AFM observations of the blend film. To analyze the results from AFM, 2D-GIWAX, and CA, it is evident that the symmetric and asymmetric fused 2-bromophenyl blocks in the central unit significantly influences the aggregation behavior of SMAs. The PM6:CHAP blend exhibits the optimal phase separation,

leading to superior J_{sc} and FF compared to the PM6:CHSPH blend.

2.5. Exciton and charge dynamics analysis

Beyond film morphology, investigating the dynamics of excitons and charge can enhance our understanding of both exciton generation and charge transport processes within the active layer. The acceptor molecules in the blend film were selectively excited at a wavelength of 760 nm, and the photoluminescence quenching efficiency (η_{PLQ}) was measured. The η_{PLQ} of the PM6:CHAPh reached 94 %, while that of the PM6:CHSPh was 88 % (See Figure S9,SI). Consistent with the above discussion, the PM6:CHAPh has an ideal phase separation size, which facilitates rapid charge transfer and thus results in a high η_{PLQ} . In contrast, the small phase separation size of the PM6:CHSPh blend hinders charge transport. Moreover, a high η_{PLQ} indicates fast charge transfer and reduces the carrier recombination rate. Subsequently, we conducted time-resolved photoluminescence (TRPL) spectroscopy on two SMAs film to explore the exciton lifetime, as illustrated in Figure S10(SI). The measured exciton lifetimes for the neat films of CHSPh and CHAPh were found to be 0.853 ns and 1.14 ns, respectively. This result indicates that CHAPh exhibits slower radiative recombination of photogenerated carriers, consistent with the higher PLQY and lower ΔE_{nr} . To explore the physical mechanisms underlying the efficiencies of various devices in greater depth, femtosecond transient absorption (fs-TA) spectroscopy was employed to analyze the exciton diffusion and dissociation behaviors within the blend films. Concentrating on the pure acceptor films, CHSPh and CHAPh exhibit a ground

state bleaching (GSB) peak with negative signals spanning wavelengths from 780 to 860 nm, along with excited - state absorption (ESA) peaks at approximately 910 nm. This phenomenon suggests the existence of photoexcited local excitons (LEs) (Fig. 4a-b) [45]. In the blend film, a wavelength of 800 nm was utilized to selectively photoexcite the acceptors. As shown in Fig. 4c, in blend of PM6:CHAPh, GSB (600–890 nm) and ESA peaks (around 920 nm) appeared rapidly after excitation and then decayed. Additionally, a GSB signal was observed around 600 nm, indicating that the excited holes transferred (HT) from the acceptor to the donor [46]. However, in the PM6:CHSPh blend, only a weak GSB peak was observed, with no significant ESA peak detected (Fig. 4d). This phenomenon is closely related to the relatively low hole mobility of CHSPh itself. Despite the presence of a large interface for exciton dissociation and charge transfer, due to the difficulty of hole migration within CHSPh, holes can hardly be transported rapidly and efficiently from the interior of CHSPh to the interface with PM6, thus failing to achieve the transfer to PM6. Meanwhile, the PM6:CHSPh blend film exhibits a large ΔE_{nr} , which implies that the energy that could have been used to drive the hole transfer is consumed by other processes. As depicted in Fig. 4e, the decay curves of this GSB signal were fitted using a biexponential function to assess the exciton dynamics. The smaller fitted parameters (τ_1 and τ_2) of the PM6:CHAPh blend films ($\tau_1 = 1.49 \pm 0.13$ ps, $\tau_2 = 17.89 \pm 1.40$ ps) imply that exciton dissociation and diffusion are more efficient compared to those in the PM6:CHSPh blend ($\tau_1 = 1.43 \pm 0.18$ ps, $\tau_2 = 21.62 \pm 2.26$ ps). This enhanced efficiency is conducive to suppressing recombination, thereby improving J_{sc} and FF.

Subsequent investigations focused on the behavior of excitons and

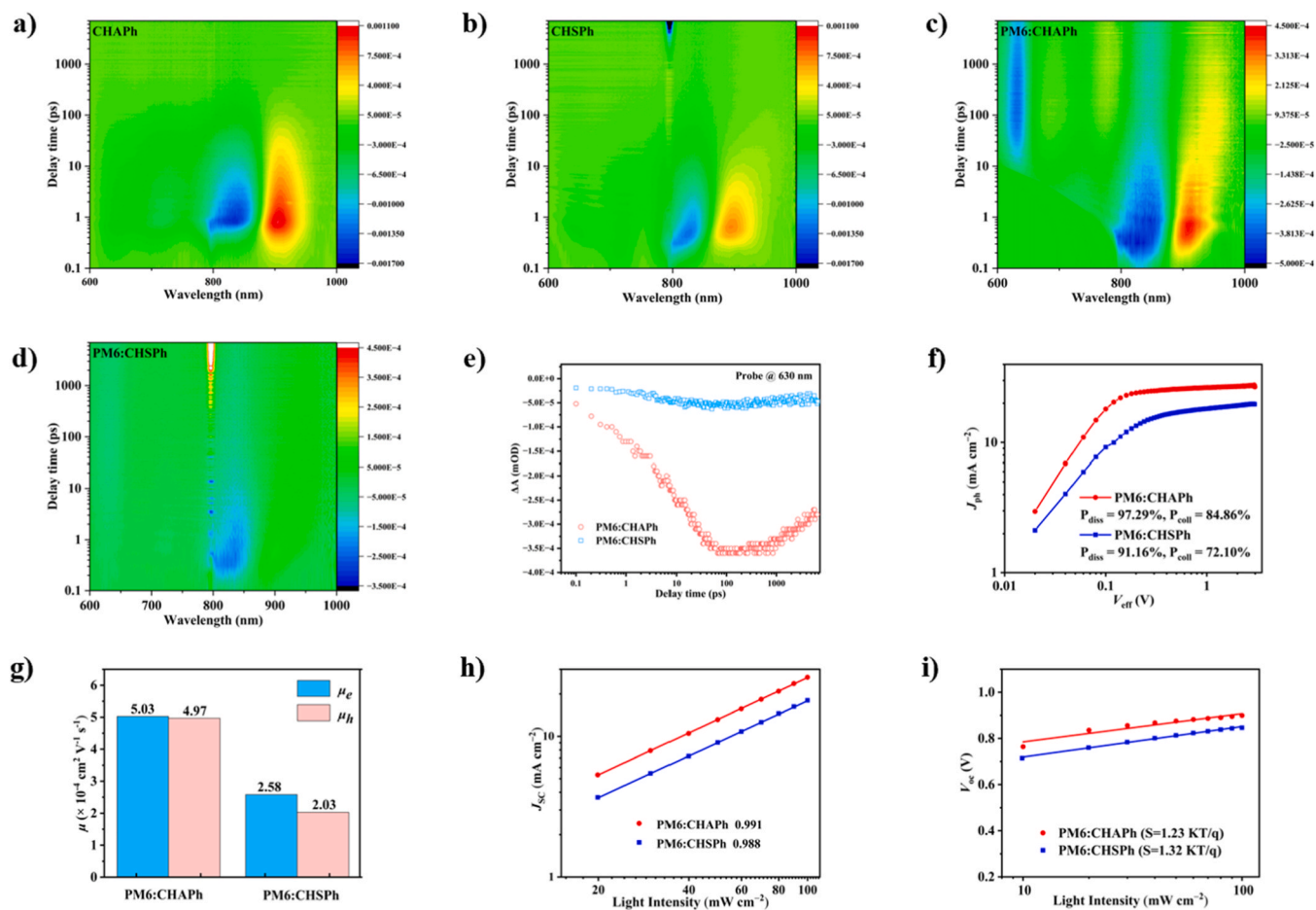


Fig. 4. a-d) Femtosecond transient absorption spectra of CHAPh, CHSPh, PM6:CHAPh, and PM6:CHSPh. e) The kinetics curves of GSB (630 nm) for the donor. f) J_{ph} versus V_{eff} characteristics. g) Histograms of the μ_e and μ_h of the OSCs based on the PM6:CHSPh and PM6:CHAPh. h) J_{sc} and i) V_{oc} versus light intensity of the optimized devices.

charge carriers to investigate the underlying reasons for the difference in PCE of two binary devices. Initial assessment of the dependence on effective voltage (V_{eff}) and photocurrent density (J_{ph}) aims to clarify the properties of charge generation and exciton separation. The OSCs based on CHAPh achieved an impressive exciton dissociation efficiency (P_{diss}) of 97.29 % and a charge collection efficiency (P_{coll}) of 84.86 %, surpass the device based on CHSPh, which exhibit P_{diss} and P_{coll} values of only 91.16 % and 72.10 %, respectively (Fig. 4f). Thereby, accounting for the observed enhancement in J_{sc} in CHAPh-based OSCs. Subsequently, charge transport properties of the two blend films were characterized using space-charge-limited current (SCLC) method using the single-carrier devices with the structure ITO/ZnO/active layer/PNDITF3N/Ag for electron mobility and ITO/PEDOT:PSS/active layer/MoO₃/Ag for hole mobility [47,48]. Compared to the PM6:CHSPh, the blend of PM6:CHAPh demonstrates improved and more balanced mobility for both electrons and holes, with values of $5.03 \times 10^{-4}/4.97 \times 10^{-4} \text{ cm}^{-2} \text{ V}^{-1} \text{ s}^{-1}$, while CHSPh displays values of $2.58 \times 10^{-4}/2.03 \times 10^{-4} \text{ cm}^{-2} \text{ V}^{-1} \text{ s}^{-1}$, as depicted in Fig. 4g. The CHAPh presents a more optimal electron-hole mobility ratio (μ_e/μ_h) of 1.01, in contrast to the 1.27 ratio found in the CHSPh. This proportionality enhances charge transfer and positively influences the FF of PM6:CHAPh devices. In OSCs, the two primary channels for charge recombination that contribute to decreased FFs and PCEs are bimolecular recombination and trap-assisted recombination. An evaluation of the dependence of J_{sc} and V_{oc} on light intensity reveals that the effect of bimolecular recombination on both types of binary OSCs is minimal (Fig. 4h). Additionally, the CHAPh-based OSC exhibits a lower trap-assisted recombination level compared to that of CHSPh (Fig. 4i), which is attributed to the highly ordered nanostructures formed in CHAPh blends, which facilitate efficient exciton dissociation while effectively suppressing trap-assisted recombination through reduced grain boundary defect density.

3. Conclusion

In summary, we designated two novel SMAs, named CHSPh and CHAPh, and investigated the effects of symmetric versus asymmetric conjugated extensions on the central unit. It demonstrates that the asymmetric fused 2-bromobenzene significantly influences the aggregation characteristics of the SMAs, leading to an enhancement in the PLQY without compromising the electron mobility within the acceptor phase. Furthermore, morphological analysis indicate that the asymmetric fused extensions greatly improve acceptor crystallinity and effectively reduce phase separation, thereby facilitating rapid charge transport and minimizing recombination. Consequently, the PM6:CHAPh blend achieved an impressive PCE of 19.35 %, with an E_{loss} measured at 0.508 eV and ΔE_{nr} as low as 0.180 eV. Therefore, the incorporation of asymmetric fused conjugated extensions into CH-series SMAs presents a promising strategy for reducing E_{loss} , and pave a way for further advancements in the designing for high efficiency materials in OSCs.

Author contributions

J. Wang conducted the acceptor synthesis experiments and wrote the original paper. **X. Chen**, fabricated and characterized the photovoltaic devices. **W. Zhao** and **G. Long** carried out the theoretical computation. **J. Yang** conducted the CA and NMR measurement. **X. Wan**, **C. Li** and **Y. Chen** supervised and directed this project. All authors discussed the results and commented on the manuscript.

CRediT authorship contribution statement

Li Chenxi: Investigation. **Yao Zhaoyang**: Investigation. **Chen Yongsheng**: Writing – review & editing, Supervision, Funding acquisition. **Wan Xiangjian**: Writing – review & editing, Supervision, Funding acquisition. **Zhao Wenkai**: Investigation. **Chen Xin**: Investigation.

Long Guankui: Investigation. **Yang Jiong**: Investigation. **Wang Jie**: Writing – original draft, Investigation, Data curation, Conceptualization.

Declaration of Competing Interest

The authors declare that they have no known competing financial interests or personal relationships that could have appeared to influence the work reported in this paper.

Acknowledgements

The authors gratefully acknowledge the financial support from National Natural Science Foundation (52025033, 52373189, 22361132530) and Ministry of Science and Technology of China (2022YFB4200400).

Appendix A. Supporting information

Supplementary data associated with this article can be found in the online version at doi:10.1016/j.nanoen.2025.111028.

Data availability

Data will be made available on request.

References

- [1] O. Inganäs, Organic photovoltaics over three decades, *Adv. Mater.* 30 (2018) 1800388, <https://doi.org/10.1002/adma.201800388>.
- [2] Z. Zheng, E. He, J. Wang, Z. Qin, T. Niu, F. Guo, S. Gao, Z. Ma, L. Zhao, X. Lu, Q. Xue, Y. Cao, G.T. Mola, Y. Zhang, Revealing the role of solvent additives in morphology and energy loss in benzodifuran polymer-based non-fullerene organic solar cells, *J. Mater. Chem. A* 9 (2021) 26105–26112, <https://doi.org/10.1039/d1ta08893a>.
- [3] H. Yao, J. Hou, Recent advances in single-junction organic solar cells, *Angew. Chem. Int. Ed.* 61 (2022) e20220, <https://doi.org/10.1002/anie.202209021>.
- [4] S. Li, Z. Li, X. Wan, Y. Chen, Recent progress in flexible organic solar cells, *eScience* 3 (2023) 100085, <https://doi.org/10.1016/j.esci.2022.10.010>.
- [5] J.D. Servaites, M.A. Ratner, T.J. Marks, Organic solar cells: a new look at traditional models, *Energy Environ. Sci.* 4 (2011) 4410–4422. (<https://doi.org/10.1039/c1ee01663f>).
- [6] A.J. Heeger, 25th Anniversary article: bulk heterojunction solar cells: understanding the mechanism of operation, *Adv. Mater.* 26 (2013) 10–28, <https://doi.org/10.1002/adma.201304373>.
- [7] J. Hou, O. Inganäs, R.H. Friend, F. Gao, Organic solar cells based on non-fullerene acceptors, *Nat. Mater.* 17 (2018) 119–128, <https://doi.org/10.1038/nmat5063>.
- [8] D. Yang, Y. Wang, T. Sano, F. Gao, H. Sasabe, J. Kido, A minimal non-radiative recombination loss for efficient non-fullerene all-small-molecule organic solar cells with a low energy loss of 0.54 eV and high open-circuit voltage of 1.15 V, *J. Mater. Chem. A* 6 (2018) 13918–13924, <https://doi.org/10.1039/c8ta04665d>.
- [9] J. Gao, N. Yu, Z. Chen, Y. Wei, C. Li, T. Liu, X. Gu, J. Zhang, Z. Wei, Z. Tang, X. Hao, F. Zhang, X. Zhang, H. Huang, Over 19.2% efficiency of organic solar cells enabled by precisely tuning the charge transfer state via donor alloy strategy, *Adv. Sci.* 9 (2022) 2203606, <https://doi.org/10.1002/adv.202203606>.
- [10] H. Gao, Q. Li, B. Fan, Z. Bi, W. Jiang, S. Zhang, Q. Fan, T. Chen, F.R. Lin, B. Kan, D. Lei, W. Ma, A.K.Y. Jen, Regulation of side-chain symmetry for delaying triplet formation and suppressing non-radiative loss in organic solar cells, *Adv. Energy Mater.* (2024) 24031, <https://doi.org/10.1002/aenm.202403121>.
- [11] W. Gao, T. Liu, J. Li, Y. Xiao, G. Zhang, Y. Chen, C. Zhong, X. Lu, H. Yan, C. Yang, Simultaneously increasing open-circuit voltage and short-circuit current to minimize the energy loss in organic solar cells via designing asymmetrical non-fullerene acceptor, *J. Mater. Chem. A* 7 (2019) 11053–11061, <https://doi.org/10.1039/c9ta02283j>.
- [12] Z. Luo, T. Liu, Y. Wang, G. Zhang, R. Sun, Z. Chen, C. Zhong, J. Wu, Y. Chen, M. Zhang, Y. Zou, W. Ma, H. Yan, J. Min, Y. Li, C. Yang, Reduced energy loss enabled by a chlorinated thiophene-fused ending-group small molecular acceptor for efficient nonfullerene organic solar cells with 13.6% efficiency, *Adv. Energy Mater.* 9 (2019) 1900041, <https://doi.org/10.1002/aenm.201900041>.
- [13] Y. Qin, S. Zhang, Y. Xu, L. Ye, Y. Wu, J. Kong, B. Xu, H. Yao, H. Ade, J. Hou, Reduced nonradiative energy loss caused by aggregation of nonfullerene acceptor in organic solar cells, *Adv. Energy Mater.* 9 (2019) 1901823, <https://doi.org/10.1002/aenm.201901823>.
- [14] X. Gu, Y. Wei, R. Zeng, J. Lv, Y. Hou, N. Yu, S. Tan, Z. Wang, C. Li, Z. Tang, Q. Peng, F. Liu, Y. Cai, X. Zhang, H. Huang, Suppressing exciton–vibration coupling via intramolecular noncovalent interactions for low-energy-loss organic solar cells, *Angew. Chem. Int. Ed.* (2024) e202418926, <https://doi.org/10.1002/anie.202418926>.

- [15] N. Wei, Y. Guo, H. Song, Y. Liu, H. Lu, Z. Bo, Reducing non-radiative energy losses in non-fullerene organic solar cells, *ChemSusChem* (2024) e202402169, <https://doi.org/10.1002/cssc.202402169>.
- [16] A. Wadsworth, M. Moser, A. Marks, M.S. Little, N. Gasparini, C.J. Brabec, D. Baran, I. McCulloch, Critical review of the molecular design progress in non-fullerene electron acceptors towards commercially viable organic solar cells, *Chem. Soc. Rev.* 48 (2019) 1596–1625, <https://doi.org/10.1039/c7cs00892a>.
- [17] Y. Xie, T. Li, J. Guo, P. Bi, X. Xue, H.S. Ryu, Y. Cai, J. Min, L. Huo, X. Hao, H. Y. Woo, X. Zhan, Y. Sun, Ternary organic solar cells with small nonradiative recombination loss, *ACS Energy Lett.* 4 (2019) 1196–1203, <https://doi.org/10.1021/acsenenergylett.9b00681>.
- [18] W. Gao, H. Fu, Y. Li, F. Lin, R. Sun, Z. Wu, X. Wu, C. Zhong, J. Min, J. Luo, H. Y. Woo, Z. Zhu, A.K.Y. Jen, Asymmetric acceptors enabling organic solar cells to achieve an over 17% efficiency: conformation effects on regulating molecular properties and suppressing nonradiative energy loss, *Adv. Energy Mater.* 11 (2020) 20033177, <https://doi.org/10.1002/aenm.202003177>.
- [19] C. He, Y. Li, Y. Liu, Y. Li, G. Zhou, S. Li, H. Zhu, X. Lu, F. Zhang, C.-Z. Li, H. Chen, Near infrared electron acceptors with a photoresponse beyond 1000 nm for highly efficient organic solar cells, *J. Mater. Chem. A* 8 (2020) 18154–18161, <https://doi.org/10.1039/d0ta06907h>.
- [20] S. Liu, J. Yuan, W. Deng, M. Luo, Y. Xie, Q. Liang, Y. Zou, Z. He, H. Wu, Y. Cao, High-efficiency organic solar cells with low non-radiative recombination loss and low energetic disorder, *Nat. Photonics* 14 (2020) 300–305, <https://doi.org/10.1038/s41566-019-0573-5>.
- [21] C. Li, J. Zhou, J. Song, J. Xu, H. Zhang, X. Zhang, J. Guo, L. Zhu, D. Wei, G. Han, J. Min, Y. Zhang, Z. Xie, Y. Yi, H. Yan, F. Gao, F. Liu, Y. Sun, Non-fullerene acceptors with branched side chains and improved molecular packing to exceed 18% efficiency in organic solar cells, *Nat. Energy* 6 (2021) 605–613, <https://doi.org/10.1038/s41560-021-00820-x>.
- [22] Y. Li, Y. Zhang, X. Zuo, Y. Lin, Organic photovoltaic electron acceptors showing aggregation-induced emission for reduced nonradiative recombination, *Chem. Commun.* 57 (2021) 5135–5138, <https://doi.org/10.1039/d1cc01170g>.
- [23] Z. Xia, J. Zhang, X. Gao, W. Song, J. Ge, L. Xie, X. Zhang, Z. Liu, Z. Ge, Fine-tuning the dipole moment of asymmetric non-fullerene acceptors enabling efficient and stable organic solar cells, *ACS Appl. Mater. Interfaces* 13 (2021) 23983–23992, <https://doi.org/10.1021/acsmi.1c02652>.
- [24] Y. Zeng, D. Li, Z. Xiao, H. Wu, Z. Chen, T. Hao, S. Xiong, Z. Ma, H. Zhu, L. Ding, Q. Bao, Exploring the charge dynamics and energy loss in ternary organic solar cells with a fill factor exceeding 80%, *Adv. Energy Mater.* 11 (2021) 2101338, <https://doi.org/10.1002/aenm.202101338>.
- [25] T. Chen, S. Li, Y. Li, Z. Chen, H. Wu, Y. Lin, Y. Gao, M. Wang, G. Ding, J. Min, Z. Ma, H. Zhu, L. Zuo, H. Chen, Compromising charge generation and recombination of organic photovoltaics with mixed diluent strategy for certified 19.4% efficiency, *Adv. Mater.* 35 (2023) 2300400, <https://doi.org/10.1002/adma.202300400>.
- [26] Y. Dong, R. Zheng, D. Qian, T.H. Lee, H.L. Bristow, P. Shakya Tuladhar, H. Cha, J. R. Durrant, Activationless charge transfer drives photocurrent generation in organic photovoltaic blends independent of energetic offset, *J. Am. Chem. Soc.* 146 (2024) 33579–33586, <https://doi.org/10.1021/jacs.4c11114>.
- [27] Y. Shi, Y. Chang, K. Lu, Z. Chen, J. Zhang, Y. Yan, D. Qiu, Y. Liu, M.A. Adil, W. Ma, X. Hao, L. Zhu, Z. Wei, Small reorganization energy acceptors enable low energy losses in non-fullerene organic solar cells, *Nat. Commun.* 13 (2022) 3256, <https://doi.org/10.1038/s41467-022-30927-y>.
- [28] X. Wu, Y. Gong, X. Li, S. Qin, H. He, Z. Chen, T. Liang, C. Wang, D. Deng, Z. Bi, W. Ma, L. Meng, Y. Li, Inner side chain modification of small molecule acceptors enables lower energy loss and high efficiency of organic solar cells processed with non-halogenated solvents, *Angew. Chem. Int. Ed.* (2024) e202416016, <https://doi.org/10.1002/anie.202416016>.
- [29] P. Xue, A.M. Calascibetta, K. Chen, K.E. Thorn, Y. Jiang, J. Shi, B. Jia, M. Li, J. Xin, G. Cai, R. Yang, H. Lu, S. Mattiello, Y. Liu, Z. Tang, W. Ma, X. Lu, Q. Meng, J. M. Hodgkiss, L. Beverina, R.P.S. Han, X. Zhan, Enhancing exciton diffusion by reducing energy disorder in organic solar cells, *J. Mater. Chem. A* 10 (2022) 24073–24083, <https://doi.org/10.1039/d2ta07113d>.
- [30] L. Zhang, D. Deng, K. Lu, Z. Wei, Optimization of charge management and energy loss in all-small-molecule organic solar cells, *Adv. Mater.* 36 (2023) 2302915, <https://doi.org/10.1002/adma.202302915>.
- [31] X. Cao, P. Wang, X. Jia, W. Zhao, H. Chen, Z. Xiao, J. Li, X. Bi, Z. Yao, Y. Guo, G. Long, C. Li, X. Wan, Y. Chen, Rebuilding peripheral F, Cl, Br footprints on acceptors enables binary organic photovoltaic efficiency exceeding 19.7%, *Angew. Chem. Int. Ed.* (2024) e202417244, <https://doi.org/10.1002/anie.202417244>.
- [32] X. Si, Y. Huang, W. Shi, R. Wang, K. Ma, Y. Zhang, S. Wu, Z. Yao, C. Li, X. Wan, Y. Chen, Achieving organic solar cells with an efficiency of 18.80% by reducing nonradiative energy loss and tuning active layer morphology, *Adv. Funct. Mater.* 33 (2023) 2306471, <https://doi.org/10.1002/adfm.202306471>.
- [33] Y. Sun, L. Wang, C. Guo, J. Xiao, C. Liu, C. Chen, W. Xia, Z. Gan, J. Cheng, J. Zhou, Z. Chen, J. Zhou, D. Liu, T. Wang, W. Li, π -Extended nonfullerene acceptor for compressed molecular packing in organic solar cells to achieve over 20% efficiency, *J. Am. Chem. Soc.* 146 (2024) 12011–12019, <https://doi.org/10.1021/jacs.4c01503>.
- [34] J. Wang, H. Chen, X. Xu, Z. Ma, Z. Zhang, C. Li, Y. Yang, J. Wang, Y. Zhao, M. Zhang, X. Wan, Y. Lu, Y. Chen, An acceptor with an asymmetric and extended conjugated backbone for high-efficiency organic solar cells with low nonradiative energy loss, *J. Mater. Chem. A* 10 (2022) 16714–16721, <https://doi.org/10.1039/d2ta03956g>.
- [35] Z. Yao, X. Cao, X. Bi, T. He, Y. Li, X. Jia, H. Liang, Y. Guo, G. Long, B. Kan, C. Li, X. Wan, Y. Chen, Complete peripheral fluorination of the small-molecule acceptor in organic solar cells yields efficiency over 19%, *Angew. Chem. Int. Ed.* 62 (2023) e202312630, <https://doi.org/10.1002/anie.202312630>.
- [36] H. Liang, X. Bi, H. Chen, T. He, Y. Lin, Y. Zhang, K. Ma, W. Feng, Z. Ma, G. Long, C. Li, B. Kan, H. Zhang, O.A. Raktin, X. Wan, Z. Yao, Y. Chen, A rare case of brominated small molecule acceptors for high-efficiency organic solar cells, *Nat. Commun.* 14 (2023) 4707, <https://doi.org/10.1038/s41467-023-40423-6>.
- [37] S. Guan, Y. Li, C. Xu, N. Yin, C. Xu, C. Wang, M. Wang, Y. Xu, Q. Chen, D. Wang, L. Zuo, H. Chen, Self-assembled interlayer enables high-performance organic photovoltaics with power conversion efficiency exceeding 20%, *Adv. Mater.* 36 (2024) 2400342, <https://doi.org/10.1002/adma.202400342>.
- [38] X. Li, R. Peng, Y. Qiu, Y. Zhang, J. Shi, S. Gao, H. Liu, F. Jin, Z. Ge, Selenization strategy of phenazine-based non-fullerene acceptors promotes photon harvesting and reduces voltage loss in organic solar cells, *Adv. Funct. Mater.* 35 (2024) 2413259, <https://doi.org/10.1002/adfm.202413259>.
- [39] J. Wu, D. Yang, Q. Wang, L. Yang, H. Sasabe, T. Sano, J. Kido, Z. Lu, Y. Huang, Central dicyanomethylene-substituted unsymmetrical squaraines and their application in organic solar cells, *J. Mater. Chem. A* 6 (2018) 5797–5806, <https://doi.org/10.1039/c8ta00750k>.
- [40] K. Liu, Y. Jiang, F. Liu, G. Ran, M. Wang, W. Wang, W. Zhang, Z. Wei, J. Hou, X. Zhu, The critical isomerization effect of core bromination on nonfullerene acceptors in achieving high-performance organic solar cells with low energy loss, *Adv. Mater.* (2024) 2413376, <https://doi.org/10.1002/adma.202413376>.
- [41] Ce Zhang, R. Zheng, H. Huang, G. Ran, W. Liu, Q. Chen, B. Wu, H. Wang, Z. Luo, W. Zhang, W. Ma, Z. Bo, C. Yang, High-performance ternary organic solar cells with enhanced luminescence efficiency and miscibility enabled by two compatible acceptors, *Adv. Energy Mater.* 14 (2024) 2303756, <https://doi.org/10.1002/aenm.202303756>.
- [42] J. Guo, X. Cao, Z. Xu, T. He, X. Bi, Z. Yao, Y. Guo, G. Long, C. Li, X. Wan, Y. Chen, Root-cause analyses for 3D intermolecular packing network formation in central unit extended small molecule acceptors, *J. Mater. Chem. A* 13 (2025) 356–367, <https://doi.org/10.1039/d4ta07485h>.
- [43] Y. Gong, T. Zou, X. Li, S. Qin, G. Sun, T. Liang, R. Zhou, J. Zhang, J. Zhang, L. Meng, Z. Wei, Y. Li, C-shaped ortho-benzodipyrrole-based acceptors with different electronic effects of top substituents for as-cast green-solvent processed high-performance organic solar cells, *Energy Environ. Sci.* 17 (2024) 6844–6855, <https://doi.org/10.1039/d4ee02467b>.
- [44] L. Zhang, H. Zhou, Y. Xie, W. Xu, H. Tian, X. Zhao, Y. Ni, S.Y. Jeong, Y. Zou, X. Zhu, X. Ma, H.Y. Woo, F. Zhang, Cascaded energy and charge transfer synergistically prompting 18.7% efficiency of layered organic solar cells with 1.48eV bandgap, *Adv. Energy Mater.* (2024) 2404718, <https://doi.org/10.1002/aenm.202404718>.
- [45] Z. Luo, W. Wei, R. Ma, G. Ran, M.H. Jee, Z. Chen, Y. Li, W. Zhang, H.Y. Woo, C. Yang, Approaching 20% efficiency in ortho-xylene processed organic solar cells by a benzo[a]phenazine-core-based 3d network acceptor with large electronic coupling and long exciton diffusion length, *Adv. Mater.* (2024) 2407517, <https://doi.org/10.1002/adma.202407517>.
- [46] X. Si, W. Shi, R. Wang, W. Zhao, Z. Suo, Z. Fu, G. Long, X. Hao, Z. Yao, X. Wan, C. Li, Y. Chen, Suppressing non-radiative recombination and tuning morphology via central core asymmetric substitution for efficient organic solar cells, *Nano Energy* 131 (2024) 110204, <https://doi.org/10.1016/j.nanoen.2024.110204>.
- [47] H. Tian, Y. Ni, W. Zhang, Y. Xu, B. Zheng, S.Y. Jeong, S. Wu, Z. Ma, X. Du, X. Hao, H.Y. Woo, L. Huo, X. Ma, F. Zhang, Over 19.2% efficiency of layer-by-layer organic photovoltaics enabled by a highly crystalline material as an energy donor and nucleating agent, *Energy Environ. Sci.* 17 (2024) 5173–5182, <https://doi.org/10.1039/d4ee01717j>.
- [48] L. Zhang, M. Zhang, Y. Ni, W. Xu, H. Zhou, S. Ke, H. Tian, S.Y. Jeong, H.Y. Woo, W.-Y. Wong, X. Ma, F. Zhang, Over 17.1% or 18.2% efficiency of layer-by-layer all-polymer solar cells via incorporating efficient π - π complexes as energy donor additive, *ACS Mater. Lett.* 6 (2024) 2964–2973, <https://doi.org/10.1021/acsmaterlett.4c00848>.



Jie Wang is a Ph.D. candidate under the supervision of Prof. Xiangjian Wan at the College of Chemistry, Nankai University. He received his Master degree in Materials and Chemical Engineering from Nankai University in 2023 and a Bachelor degree in Chemical Engineering and Technology from Taiyuan Industrial College in 2019. His current research focuses on the design and synthesis of organic photovoltaic materials.



Xin Chen is a Ph.D. candidate under the supervision of Prof. Xiangjian Wan at the College of Chemistry, Nankai University. Her received his BSc degree in materials chemistry from Henan University in 2021. Her research focuses on organic photovoltaic device fabrication and optimization.



Zhaoyang Yao received his Ph.D. degree from Changchun Institute of Applied Chemistry (CIAC), Chinese Academy of Sciences in 2016. Currently, he is a professor in Department of Chemistry, Nankai University. His main research activities focus on the development of organic functional materials for various optoelectronic applications.



Wenkai Zhao is a Master candidate under the supervision of Prof. Guankui Long at Nankai University. He received his BSc degree in materials chemistry from Civil Aviation University of China in 2019. His research focuses on the simulation of organic solar cell morphology.



Chenxi Li received his Ph.D. degree in Organic Chemistry from Nankai University, China, in 1990. Currently, he is a professor of Chemistry, Nankai University. His research interests focus on organic functional material design and synthesis.



Jiong Yang is a Master candidate under the supervision of Prof. Xiangjian Wan at Nankai University. He received his BSc degree in Material Chemistry from East China University of Science and Technology in 2024. His research focuses on the design and synthesis of organic photovoltaic materials.



Xiangjian Wan received his Ph.D. degree in Organic Chemistry from Nankai University, China, in 2006. Currently, he is a professor of Chemistry, Nankai University. His research interests focus on organic functional material design and application, especially on OPV material design and device optimization.



Guankui Long, Professor at Nankai University, earned his B.S. from Lanzhou University (2009) and Ph.D. from Nankai University under Prof. Yongsheng Chen. He conducted post-doctoral research at Tianjin Collaborative Innovation Center (Profs. Guan/Chen), University of Toronto (Prof. Sargent), and NTU (Profs. Gao/Soci). Since 2020, he leads an independent research group at Nankai University focusing on chemistry and materials science.



Yongsheng Chen received his Ph.D. in chemistry from the University of Victoria in 1997. From 2003, he has been a Chair Professor at Nankai University. His main research interests focus on carbon-based nanomaterials and organic functional materials for green energy application.